THE ASTRONOMICAL JOURNAL, 171:184 (15pp), 2026 March
https://doi.org/10.3847/1538-3881/ae38d5

Nine Years of UVIT: Assessing Sensitivity Variation

Akanksha Dagore[1], Prajwel Joseph[1], S. N. Tandon[2], Annapurni Subramaniam[1], S. K. Ghosh[3], and C. S. Stalin[1]
[1] Indian Institute of Astrophysics, Koramangala II Block, Bangalore 560034, India; akankshadagore@gmail.com
[2] Inter-University Center for Astronomy and Astrophysics, Pune 411007, India
[3] Tata Institute of Fundamental Research, Mumbai 400005, India

Received 2025 May 15; revised 2025 December 16; accepted 2025 December 27; published 2026 February 23

Abstract

The Ultra-Violet Imaging Telescope (UVIT) is one of the five payloads on board the first Indian multiwavelength astronomical observatory, AstroSat, launched by the Indian Space Research Organisation on 2015 September 28. UVIT, designed for simultaneous imaging in the far-ultraviolet (FUV; 1300−1800 Å) and near-ultraviolet (NUV; 2000−3000 Å) channels, has completed 9 yr in orbit in 2024 despite the failure of the NUV channel in 2018. As the FUV optics is subject to possible reduction in sensitivity due to microscopic amounts of contaminants, we used the FUV data acquired by UVIT over the past 9 yr on the open cluster NGC 188 and the white dwarf HZ 4 to study sensitivity variations in the UVIT FUV channel. Our findings indicate no significant reduction in the sensitivity of the FUV channel over the last 9 yr, with no significant episodic variations due to unknown causes.

Unified Astronomy Thesaurus concepts: Ultraviolet telescopes (1743); Open star clusters (1160); Ultraviolet observatories (1739)

1. Introduction

The Ultra-Violet Imaging Telescope (UVIT) is one of the five payloads on board AstroSat (K. P. Singh et al. 2014; P. Agrawal 2017), India's first space observatory targeted toward carrying out simultaneous multiwavelength observations launched on 28 September 2015. AstroSat is capable of observing in the ultraviolet (UV), visible (VIS), and X-ray spectral bands with the help of its five scientific payloads, namely, UVIT, the Soft X-ray imaging Telescope, the Large Area X-ray Proportional Counter, the Cadmium Zinc Telluride Imager, and the Scanning Sky Monitor. While the other four payloads observe in the X-ray window, UVIT performs simultaneous observations for a given region of the sky in far-ultraviolet (FUV; 1300–1800 Å), near-ultraviolet (NUV; 2000−3000 Å), and VIS (3200−5500 Å) channels.

UVIT consists of twin Ritchey–Chrétien telescopes, each with a primary and a secondary mirror of ∼375 and ∼140 mm diameter, respectively, along with a channel-filter configuration and a detector system. Each channel is equipped with a set of filters to select a narrower bandpass in which the intensified imaging detectors can operate in two distinct modes, namely, high-gain photon counting (PC) mode and low-gain integration (INT) mode. The FUV and NUV channels perform observations in the PC mode, with a frame rate of ∼29 frames per second. The VIS channel, on the other hand, works in the low-gain INT mode, which gives out a reduced frame rate (∼1 frame per second). The VIS channel is used to estimate the spacecraft pointing drift (S. K. Ghosh et al. 2021). For the two UV channels, UVIT has a spatial resolution of $\sim1\farcs5$ FWHM and a field of view of $\sim28'$ diameter. The C-MOS imagers of the detectors have a size of 512 × 512 pixels. Observations can also be carried out in already defined, narrower window settings at faster frame rates.

The expected mission duration for AstroSat was planned to be 5 yr (K. P. Singh et al. 2014); however, as of 2024 September, AstroSat has completed 9 yr in orbit. The UVIT NUV channel became nonoperational during this period on 2018 March 30. Despite the failure of the NUV channel, the FUV and VIS channels continue to function as intended. However, given its time in orbit, there exists a possibility that UVIT could have experienced a reduction in sensitivity. Possible factors can include degradation of reflectivity due to atomic oxygen (B. Banks et al. 2004), chemical contamination of the optical surfaces due to charged particles and UV radiation assisted reactions (G. Nahor et al. 1993), and accumulation of space dust and debris (D. Garoli et al. 2020). Therefore, all these issues raise a need to investigate for any sensitivity degradation in UVIT.

In a previous study, S. N. Tandon et al. (2020) found no significant degradation in the sensitivity of the FUV and NUV channels of UVIT, using stars in open cluster NGC 188 observations between 2015 December 31 and 2018 October 23. Since then, several years have passed, highlighting the need for new analysis. With the NUV channel nonfunctional since 2018, only the FUV channel requires sensitivity checks. To assess potential sensitivity variations in the FUV channel, frequent observations of a stable source spanning the lifetime of UVIT are necessary. The requirement of stability is obviously fulfilled by the white dwarf HZ 4, which is the calibration source for photometry with UVIT. However, unlike NGC 188, HZ 4 is not available for observation for all months of the year. Therefore, we use frequent observations of NGC 188 to monitor any significant variations, such as >5%, on timescales of a few months and infrequent observations of HZ 4 to monitor long-term decline at levels of 1%. By comparing flux measurements of this source at various epochs, we can identify any changes in the FUV channel's sensitivity over time.

UVIT captured its first sky image on 2015 November 30 of the open cluster NGC 188 ($\alpha = 00^{\rm h}47^{\rm m}11\fs5$, $\delta = 85^\circ14''38''$)[4] (S. K. Ghosh et al. 2021), which has been monitored ever since for the telescope's calibration and sensitivity studies, including the current one. NGC 188 observations are also conducted to

---

[4] https://simbad.u-strasbg.fr/simbad/sim-basic?Ident=NGC+188

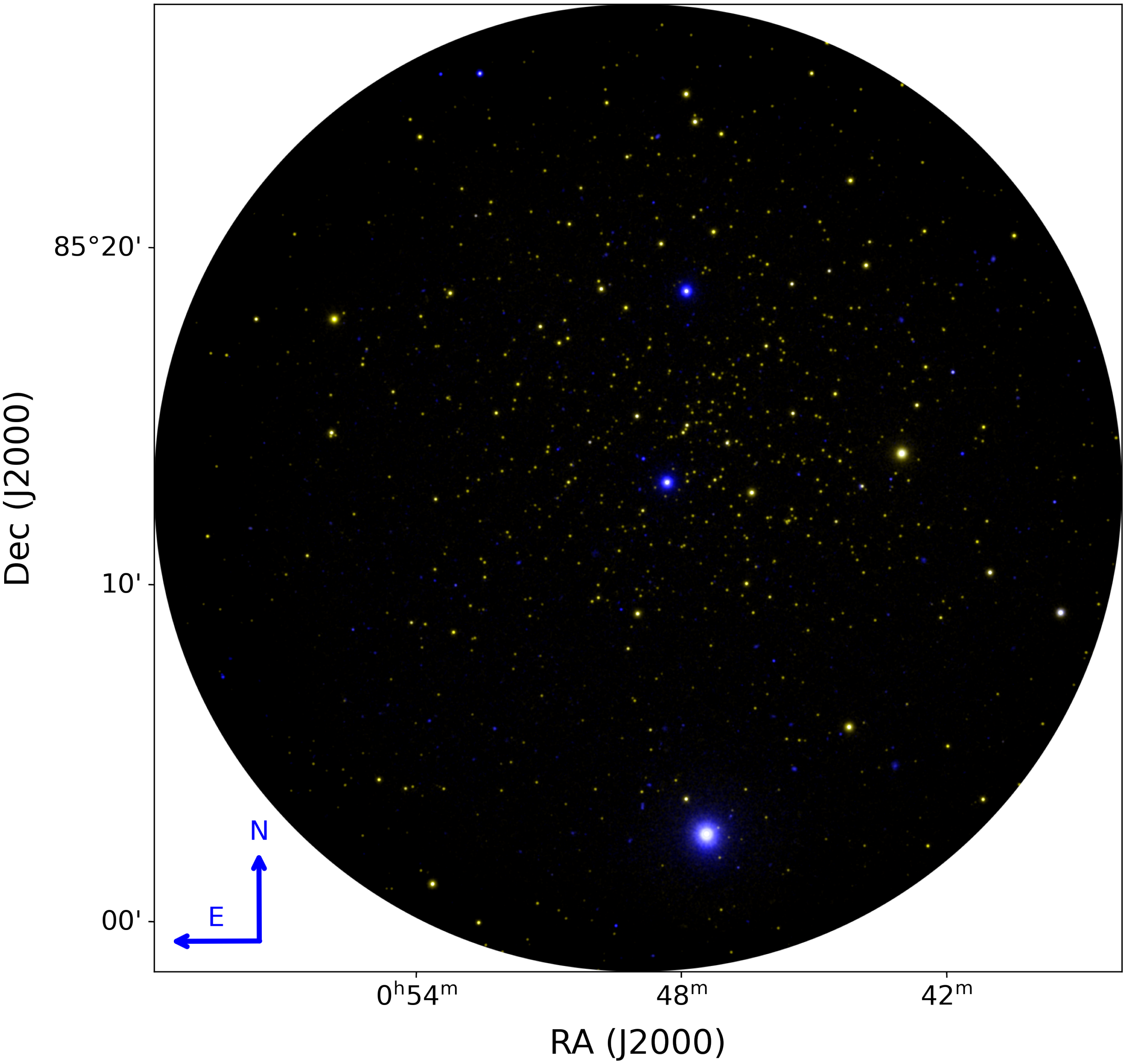

Figure 1. A pseudocolor image of the NGC 188 field. The blue and yellow colors represent the observations conducted in the UVIT's FUV F148W (exposure time = 36,484 s) and NUV N279N (exposure time = 14,954 s) filters, respectively. The image has been processed to bring out the faint features.

test UVIT's functionality after performing mitigation operations to resolve instrument problems. Furthermore, these observations have contributed to scientific studies (A. Subramaniam et al. 2016; S. Rani et al. 2021). Figure 1 illustrates a pseudocolor image of the NGC 188 field created from the FUV F148W and NUV N279N filters of UVIT. While three FUV-bright sources are visible in Figure 1, the brightest source suffers from saturation effects, and the other two were found to be variable during the course of this work. Nevertheless, this calibration source provides data to monitor any decline in sensitivity at levels below 1% over long periods of years.

Section 2 discusses the characteristics of the observational data used for the analysis. The data reduction methodology is explained in Section 3. The analysis and results are given in Section 4. Lastly, the conclusion is reported in Section 5.

2. Observational Data

The UVIT observations are planned to coincide with the orbital phase of the satellite that falls within the Earth's shadow, which blocks direct exposure from the Sun to prevent instrument damage. AstroSat covers a complete orbit around the Earth in ∼100 minutes, and any uninterrupted imaging session during this phase with a specific filter-window configuration is termed an *episode*.

The observational data for HZ 4 and NGC 188 were obtained from the AstroSat Archive of the Indian Space Science Data Centre (ISSDC).[5] The data were downloaded in the science-ready Level2 (L2) format, which was processed by

---

[5] https://astrobrowse.issdc.gov.in/astro_archive/archive/Home.jsp

Table 1
HZ 4 Observation IDs Obtained from ISSDC and Their Respective Dates of Observation, Number of Episodes, and Exposure Time in Seconds

No.	Observation ID	Date of Observation (dd-mm-yyyy)	No. of Episode Images	Exposure Time (s)
1.	C02_002T01_9000000888	16-12-2016	3	375 375 375
2.	C03_013T01_9000001586	06-10-2017	4	336 374 261 245
3.	C04_010T01_9000003158	12-09-2019	4	358 358 271 164
4.	C02_002T01_9000006092	24-02-2024	2	359 359

the L2 pipeline software (version 6.3; S. K. Ghosh et al. 2021, 2022) at the UVIT Payload Operation Centre (POC) and transferred to ISSDC for archiving and dissemination. The L2 pipeline performs a series of operations on the Level1 data and refines them into science-ready L2 data products.

Depending on the duration of the observation, the imaging sessions may be divided into episodes that span multiple orbits. The 6.3 version L2 data generated for each episode are organized and stored separately for each channel and usually consist of the following elements in FITS format:

1. image file in the instrument coordinate system (x, y);
2. image file in the astronomical coordinate system (α, δ);
3. exposure map in the astronomical coordinate system (α, δ);
4. error/noise map in the astronomical coordinate system (α, δ); and
5. a tabulated list containing information about the recorded photon events.

For the current study, 4 UVIT observations of HZ 4 and 35 of the NGC 188 field were analyzed. They span from 2016 March 22 to 2024 August 28. Many of the individual observations consist of multiple episodes, leading to 13 episode images for HZ 4 and 57 for NGC 188. We have used only FUV F148W filter imaging data and discarded those episodes with less than 130 s of exposure time. While the NGC 188 observations were obtained in the 512 × 512 pixels window mode, the HZ 4 observations were in the 200 × 200 pixels window mode. An observation taken in 200 × 200 pixels window mode provides a higher frame rate (≈180 frames per second) as compared to that with the window of 512 × 512 pixels (≈29 frames per second) and hence reduces saturation effects. Tables 1 and 2 list the observation IDs, observation dates, number of episode images, and exposure times for the HZ 4 and NGC 188 observations, respectively. Regardless of the window mode, all image products have a size of 4800 × 4800 subpixels (1 subpixel length = 1/8 detector pixel length).

Table 2
NGC 188 Observation IDs Obtained from ISSDC and Their Respective Dates of Observation, Number of Episodes, and Exposure Time in Seconds

No.	Observation ID	Date of Observation (dd-mm-yyyy)	No. of Episode Images	Exposure Time (s)
1.	T01_034T01_9000000392	22-03-2016	2	562 466
2.	G05_209T01_9000000458	18-05-2016	1	1105
3.	G05_258T01_9000000666	15-09-2016	1	621
4.	C02_016T01_9000000992	30-01-2017	1	1195
5.	C02_030T01_9000001168	16-04-2017	3	307 433 352
6.	C03_015T01_9000001788	21-12-2017	1	149
7.	T02_002T01_9000001914	23-02-2018	2	1855 1039
8.	C03_015T02_9000002008	04-04-2018	1	431
9.	C03_015T04_9000002240	20-07-2018	1	1063
10.	C03_015T04_9000002328	26-08-2018	3	255 336 541
11.	C03_015T03_9000002366	14-09-2018	3	554 424 155
12.	C03_015T04_9000002382	21-09-2018	1	1140
13.	C04_009T01_9000002448	23-10-2018	1	1140
14.	C04_009T02_9000002618	04-01-2019	1	1140
15.	C05_013T02_9000003364	13-12-2019	1	1140
16.	C05_013T03_9000003376	19-12-2019	1	508
17.	C05_013T04_9000003660	12-05-2020	1	1144
18.	T03_247T01_9000003914	05-10-2020	2	193 546
19.	C05_013T06_9000003920	15-10-2020	1	736
20.	C06_010T01_9000004504	03-07-2021	1	678
21.	C06_010T02_9000004618	02-08-2021	2	1469 875
22.	C06_010T03_9000004672	27-08-2021	2	991 1480
23.	C06_010T05_9000004736	25-10-2021	2	1558 204
24.	T04_065T01_9000004750	01-11-2021	1	163
25.	C06_010T05_9000005424	15-12-2022	3	482 1319 985
26.	C06_010T05_9000005436	23-12-2022	2	1046 1732
27.	C06_010T05_9000005484	15-01-2023	2	1435 1174

Table 2
(Continued)

No.	Observation ID	Date of Observation (dd-mm-yyyy)	No. of Episode Images	Exposure Time (s)
28.	T05_101T01_9000005578	22-04-2023 23-04-2023	2	793 212
29.	T05_101T01_9000005586	28-04-2023 29-04-2023	2	851 182
30.	C06_010T05_9000005670	30-05-2023	2	522 890
31.	C06_010T01_9000005800	29-07-2023	2	1269 227
32.	C06_010T01_9000005816	13-08-2023	2	195 390
33.	C09_011T02_9000006310	24-06-2024	1	736
34.	C09_011T03_9000006410	25-08-2024	2	732 1379
35.	C09_011T01_9000006418	28-08-2024	1	573

3. Methodology

We need to obtain the fluxes of select sources at different epochs to assess the FUV channel sensitivity variations. This section explains the steps followed to obtain source fluxes from the episode images.

3.1. Source Selection

The HZ 4 source was chosen to carry out sensitivity checks in the HZ 4 field. In all the exposures, HZ 4 remains close to the center of the field, and hence the data are minimally affected by errors in the flat-field correction. We chose three sources in the NGC 188 field. We ensured that the selected sources in the NGC 188 field did not lie outside of an 1800 subpixel radius from the image centroid, were not saturated, and, most importantly, were present in all 57 episode images. Figure 2 shows the selected sources in the NGC 188 field. The brightest source in the field was saturated, so we chose the next three brightest sources that met our criteria. We identified these three sources across all 57 episode images using the `Aafitrans` Python package (M. Beroiz et al. 2020; P. Joseph 2023), which matches centroids of the detected sources in a reference image against all remaining images (see Appendix C for details on the source detection method). The sources are located at different radii in the field, and as the field rotates over the year, they explore different parts of it. For this reason, the corresponding data are affected by any errors in the flat-field correction.

3.2. Aperture Photometry

A key step in performing aperture photometry is the subtraction of the background. The method used to generate the background maps for episode images is explained in Appendix B. Each subpixel in the background-subtracted image of an individual episode gives a measure of the photons recorded by the detector in counts per second (CPS) units. The aperture photometry was done using the `Photutils` package (L. Bradley et al. 2022). We used an aperture of 12 subpixel radius that encompasses 88.6% of the source encircled energy in the FUV channel (S. N. Tandon et al. 2020).

3.3. Applying Corrections to the Selected Source Fluxes

There are factors that can influence the calculated flux values and, therefore, must be accounted for. These arise due to the selected aperture size and the detector's inability to distinguish multiple photons falling within a small region of 3 × 3 detector pixels in a single frame (saturation effects). We applied aperture and saturation corrections to address them, respectively.

A method to correct for the saturation effects was put forward by S. N. Tandon et al. (2017) based on the idea that the incident photons falling on the detector follow a Poisson distribution. However, this method is specifically designed for source flux in CPS without flat-field correction. As the episode images have flat-field corrections, it is necessary first to reverse the flat-field correction and extract the non-flat-fielded flux in CPS before applying aperture and saturation corrections. Therefore, we applied the corrections as follows:

(i) removed flat-field corrections from the flux in CPS to get the non-flat-fielded flux in CPS;
(ii) applied aperture correction;
(iii) applied saturation correction; and
(iv) reintroduced the flat-field correction to obtain the final flat-fielded flux in CPS with aperture and saturation corrections.

The methodology for these corrections is explained in the following sections.

3.3.1. Flat-field Correction Removal

The flat fields for each filter are stored in the calibration data files, which are used by the L2 pipeline to generate L2 data. Since the L2 pipeline applies the flat-field correction before the telescope pointing drift correction, removing the flat-field correction from L2 images is not straightforward. Therefore, we adopted the following approximate approach to remove the flat-field correction.

The UVIT images have a dimension of 4800 × 4800 subpixels, while the flat fields are 512 × 512 pixels (S. K. Ghosh et al. 2022). For each source coordinate (x_s, y_s) in the instrument coordinate system image, the corresponding location in the flat-field (x_f, y_f) was calculated using the following equations:

$$x_f = 256 + \frac{x_s - x_{\text{center}}}{8}, \tag{1}$$

$$y_f = 256 + \frac{y_s - y_{\text{center}}}{8}. \tag{2}$$

Here, (x_{centre}, y_{centre}) denotes the coordinate of the field center, which serves as the reference point for mapping the image to the flat-field grid. A 21 × 21 pixel window was placed centered on (x_f, y_f) in the flat field, and the average of the pixel values within this window (FF_{avg}) was estimated. Then, the non-flat-fielded flux in CPS (CPS_{noFF}) was obtained

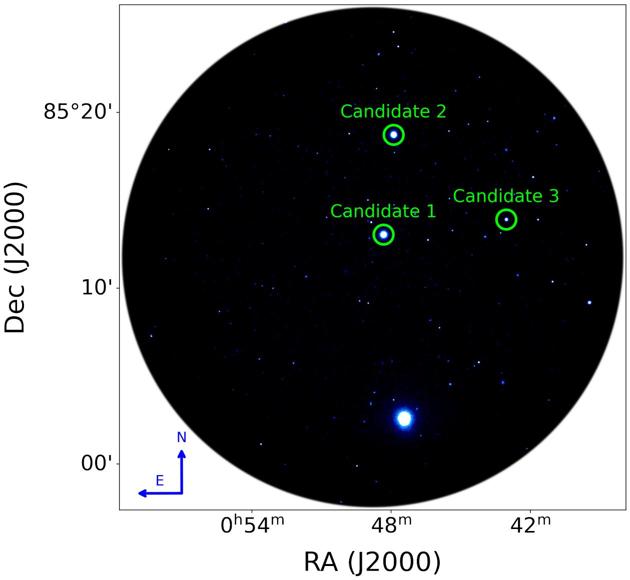

Figure 2. The three sources (green circles) selected in the NGC 188 field to carry out UVIT sensitivity checks are marked in the UVIT F148W image. The image has been processed to bring out the faint features.

using the equation

$$\mathrm{CPS_{noFF}} = \frac{\mathrm{CPS_{measured}} - \mathrm{CPS_{bkg}}}{\mathrm{FF_{avg}}}, \tag{3}$$

where $\mathrm{CPS_{measured}}$ is the measured source flux in CPS. Background maps were generated for each UVIT image (see Appendix B) and used to obtain the local background level, $\mathrm{CPS_{bkg}}$.

The uncertainty in the measured flux, $\mathrm{CPS_{measured\_error}}$, was calculated using the following equation:

$$\mathrm{CPS_{measured\_error}} = \frac{\sqrt{(\mathrm{CPS_{measured}}/FF_{\mathrm{avg}}) \times t_{\mathrm{exp}}}}{t_{\mathrm{exp}}}, \tag{4}$$

where t_{exp} is the exposure time in seconds for a given observation. Uncertainties propagated through each correction step were evaluated using $\mathrm{CPS_{measured\_error}}$.

3.3.2. Aperture Correction

S. N. Tandon et al. (2020) provide a table listing the point-source-encircled energy percentages as a function of the aperture radius in subpixels for both the NUV and FUV channels. From this table, we derived the aperture correction factor (f_{ac}) to be 100/88.6 for a 12 subpixel radius aperture in the FUV channel. The aperture corrected flux in CPS ($\mathrm{CPS_{ac}}$) was then calculated using the equation

$$\mathrm{CPS_{ac}} = \mathrm{CPS_{noFF}} \times f_{\mathrm{ac}}. \tag{5}$$

3.3.3. Saturation Correction

When multiple photons fall within a small area of 3 × 3 UVIT detector pixels during a single frame in PC mode, the detector registers them as a single photon. This leads to a saturation of the measured photon count rate. Unless the source counts per frame (CPF) $< <$ 1, the saturation effect must be corrected while estimating the photon count rate as failing to do so would underestimate the source flux. The UVIT saturation correction method for observed source CPF up to 0.6 is given by S. N. Tandon et al. (2017) and is elaborated below.

In UVIT images, the central 40 × 40 subpixels region of a source contains 97% of the source photons and is more susceptible to saturation effects than the low-count pedestal of its point-spread function profile. Therefore, we need to apply saturation correction within this region. If CPF5 denotes 97% of the observed CPF and ICPF5 represents the corresponding actual CPF using Poisson statistics, then CPF5 and ICPF5 can be related using the following equations:

$$\mathrm{CPF5} = 1 - e^{-\mathrm{ICPF5}}, \tag{6}$$

$$\mathrm{ICPF5} = -\ln(1 - \mathrm{CPF5}). \tag{7}$$

The difference between CPF5 and ICPF5 should give the ideal correction for saturation, i.e.,

$$\mathrm{ICORR} = \mathrm{ICPF5} - \mathrm{CPF5}. \tag{8}$$

However, the real correction for saturation, RCORR, is found to be different from the ideal correction, ICORR. S. N. Tandon et al. (2017) provide a relation between RCORR and ICORR as follows:

$$\mathrm{RCORR} = \mathrm{ICORR} \times (0.89 - 0.30 \times (\mathrm{ICORR})^2). \tag{9}$$

We used the above prescription to correct $\mathrm{CPS_{ac}}$ for saturation. We obtained CPF5 from $\mathrm{CPS_{ac}}$ using the equations

$$\mathrm{CPF_{ac}} = \frac{\mathrm{CPS_{ac}}}{\text{frame rate}}, \tag{10}$$

$$\mathrm{CPF5} = \mathrm{CPF}_{ac} \times 0.97. \tag{11}$$

Then, RCORR was calculated using CPF5. The saturation corrected flux in CPS ($\mathrm{CPS_{sc}}$) was obtained as

$$\mathrm{CPS_{sc}} = \mathrm{CPS_{ac}} + (\mathrm{RCORR} \times \text{frame rate}). \tag{12}$$

We have now obtained the non-flat-fielded flux in CPS with aperture and saturation corrections ($\mathrm{CPS_{sc}}$). Finally, we reintroduce the flat-field correction:

$$\mathrm{CPS_{final}} = \mathrm{CPS_{sc}} \times \mathrm{FF_{avg}}, \tag{13}$$

where $\mathrm{CPS_{final}}$ is the final corrected flux in CPS for a given source. A flow chart of the steps adopted to get the final fluxes of the point sources is given in Figure 3.

4. Sensitivity Analysis

Here we analyze the multiepoch point-source fluxes from the HZ 4 and NGC 188 fields to investigate potential variations in UVIT sensitivity. The source fluxes were calculated following the methodology described in Section 3.

4.1. HZ 4

To analyze the data, we calculated the mean source flux for each observation ID by averaging the episode-wise source fluxes within that ID (see Appendix D for the corrected flux measurements and associated uncertainties). The resulting light curve along with its best-fit line and global average are shown in Figure 4, with the line fit statistics provided in Table 3. The linear least-squares fits were weighted by the inverse square of the measurement uncertainties(i.e., 1 / $\mathrm{CPS^2_{final\_error}}$). The intercept was determined at the midpoint of the observation time period and is marked as Day 0. This

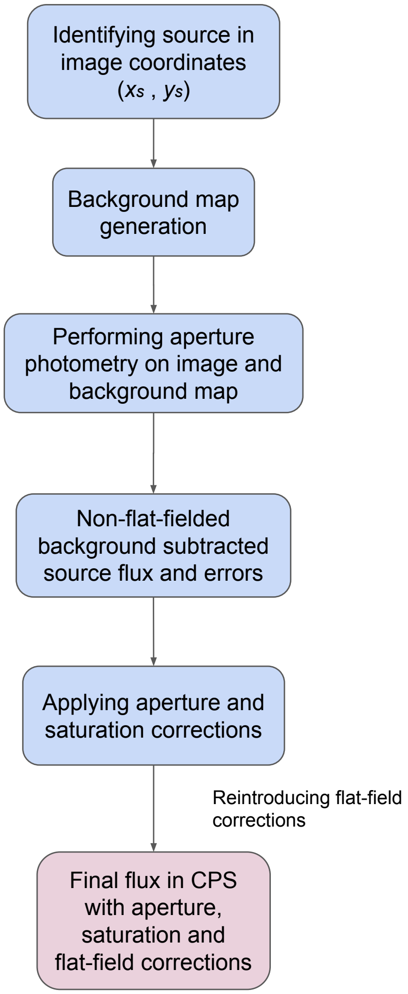

Figure 3. All steps followed to get the corrected flux for a point source.

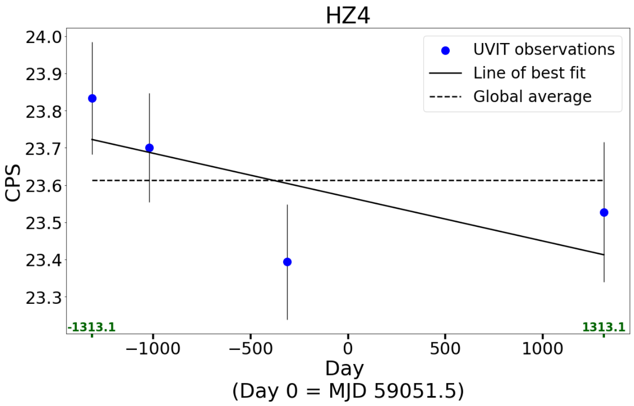

Figure 4. The FUV light curve for HZ 4. The solid and dashed lines mark the best-fit line and the global average of the data, respectively. Green minor ticks and labels mark the times of the first and last observations.

approach is adopted to compute the intercepts in all subsequent analyses presented in this paper. The best-fit line equation for HZ 4 is given by (14). In the equation, the independent variable, MJD, refers to the Modified Julian Date, while CPS (MJD) represents CPS as a function of MJD.

$$\mathrm{CPS(MJD)} = (-1 \times 10^{-4} \pm 1 \times 10^{-4})(\mathrm{MJD} - 59051.5) + 23.6 \pm 0.1. \tag{14}$$

Table 3
Line Fit Statistics for the HZ 4 FUV Data Shown in Figure 4

Source	MJD at Day 0	Slope (CPS/MJD)		Intercept at Day 0 (CPS)		Global average (CPS)	
		Value	Error	Value	Error	Value	Error
HZ 4	59051.5	−1e-04	1e-04	23.6	0.1	23.61	0.08

Although the estimated slope is negative, the large associated error introduces significant uncertainty. It is also seen that a constant value gives an acceptable fit, and we infer that the sensitivity shows no degradation. We can also put a 95% confidence upper limit on the degradation over the 9 yr as 4%.

4.2. NGC 188

The light curves of the three selected sources in the NGC 188 field are shown in Figure 5 (see Appendix D for the corrected flux measurements and associated uncertainties). From this figure, it can be observed that candidates 1 and 2 are relatively bright compared to candidate 3. All three show flux variations, particularly candidates 1 and 2, which exhibit significant changes exceeding the associated uncertainties. As the data on HZ 4 are consistent with no sensitivity degradation, we assume the same holds true for these sources. Any signal variations are, therefore, attributed to errors in flat-field correction, temporal variations in the sources themselves, or episodic unexplained variations in the FUV sensitivity. If episodic FUV sensitivity variations of unknown origin exist, the observed variability can be interpreted as an upper limit on their amplitude. It is also possible that the variability is intrinsic to the sources themselves; however, a detailed investigation of this is beyond the scope of the present work and will be addressed separately.

Using `Astrometry.net` software (D. Lang et al. 2010; see also Appendix E) and the SIMBAD Astronomical Database[6] (M. Wenger et al. 2000), candidate 1 was identified as a blue straggler star with a postasymptotic giant branch/horizontal branch companion (WOCS-5885) by A. Subramaniam et al. (2016), while candidate 2 was found to be a subdwarf (WOCS-4918; S. Rani et al. 2021). Regarding the possibility of any episodic variations in the sensitivity due to any possible unknown cause, these results indicate that these are not more than ∼5%. To address this, we computed the weighted root mean square deviations (RMSD) from the line of constant fit for the NGC 188 observations, which are provided in Table 4.

5. Summary

In 2024 September, UVIT achieved a significant milestone by completing 9 yr in orbit. As the telescope ages, it is essential to assess whether any sensitivity degradation has occurred due to various potential factors. To investigate this, we analyzed the multiepoch data from white dwarf HZ 4, the calibration source for UVIT. We also analyzed the frequent observations of the open cluster NGC 188 to check for any short-term episodic variations in sensitivity.

---

[6] https://simbad.u-strasbg.fr/simbad/

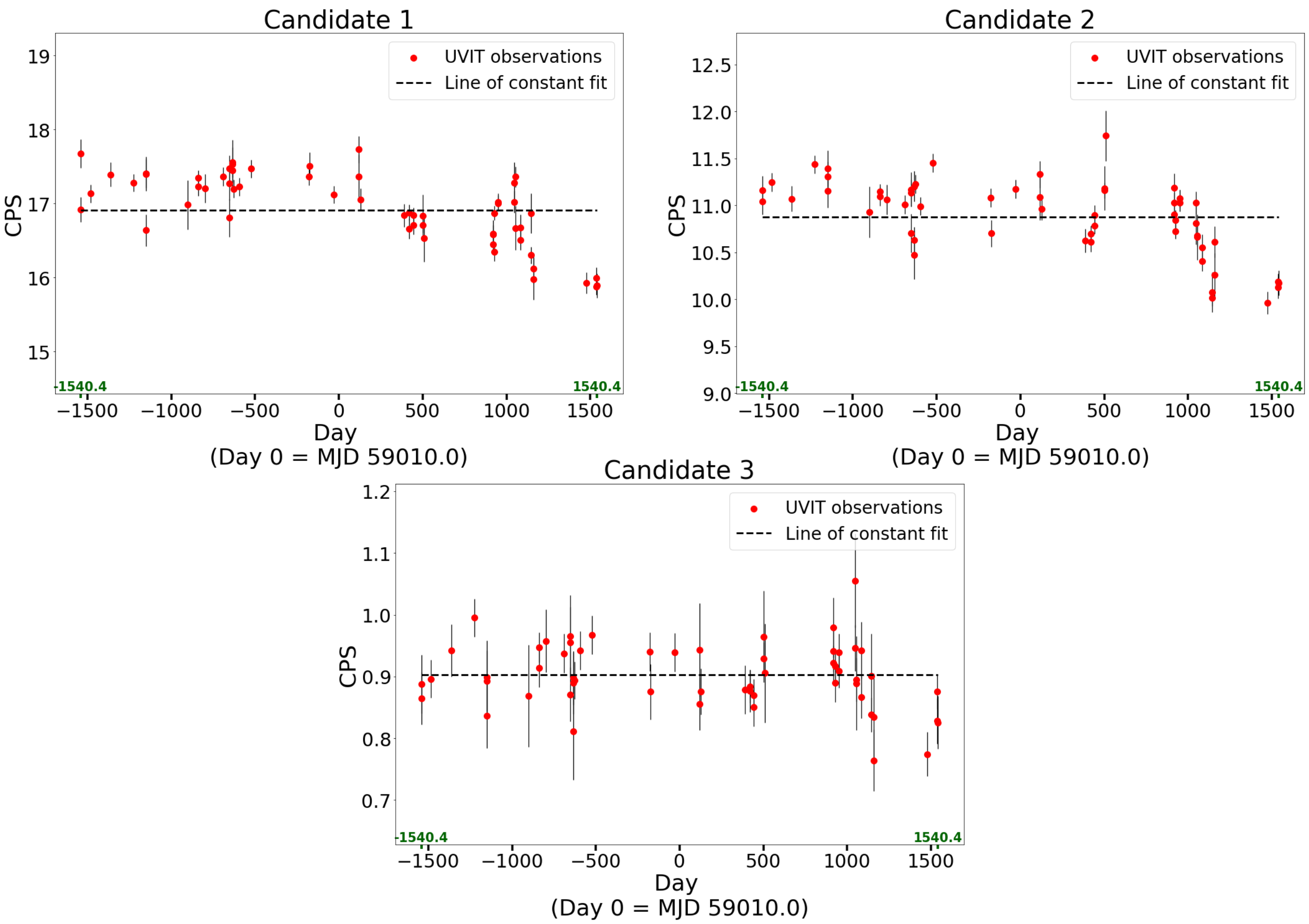

Figure 5. The FUV light curves for the selected three sources in the field of NGC 188. The dashed line marks the line of constant fit. Green minor ticks and labels mark the times of the first and last observations.

Table 4
Weighted RMSD Values from the Line of Constant Fit for the FUV Data of the Three Selected Sources from NGC 188 Shown in Figure 5

Source	Line of Constant Fit		
	(CPS)		
	Value	Error	RMSD
Candidate 1	16.91	0.06	0.463 (2.74%)
Candidate 2	10.88	0.05	0.376 (3.46%)
Candidate 3	0.902	0.006	0.046 (5.12%)

The results for HZ 4 are consistent with no degradation in sensitivity at the center of the field for the FUV channel. They also provide a 95% confidence upper limit of ∼4% on degradation over the full period of 9 yr. Based on these findings, we conclude that there is no significant degradation of sensitivity in the FUV channel. Since the sensitivity of the NUV channel is far less likely to degrade compared to the FUV channel, we infer that its sensitivity remained stable throughout its operation until 2018. As far as any possibility of a shorter-term sensitivity variability is concerned, the results on NGC 188 indicate that these are not more than ∼5%.

Acknowledgments

The UVIT project is a part of the AstroSat mission by the Indian Space Research Organisation (ISRO) and includes collaboration from the Indian Institute of Astrophysics (IIA), Bengaluru; the Indian-University Centre for Astronomy and Astrophysics (IUCAA), Pune; Tata Institute of Fundamental Research (TIFR), Mumbai; many centers of ISRO; and the Canadian Space Agency (CSA). This publication uses the data from the AstroSat mission of the Indian Space Research Organisation (ISRO), archived at the Indian Space Science Data Centre (ISSDC). This work has made use of data from the European Space Agency (ESA) mission Gaia (https://www.cosmos.esa.int/gaia), processed by the Gaia Data Processing and Analysis Consortium (DPAC; https://www.cosmos.esa.int/web/gaia/dpac/consortium). Funding for the DPAC has been provided by national institutions, in particular the institutions participating in the Gaia Multilateral Agreement. This research has made use of the SIMBAD database, operated at CDS, Strasbourg, France.

Data Availability

The data and codes that support the findings of this study are available in the repository `UVIT-sensitivity-analysis` at https://github.com/akanksha-dagore/UVIT-sensitivity-analysis (doi:10.5281/zenodo.18076974; A. Dagore et al. 2025).

Facilities: UVIT, Gaia, SIMBAD.

Software: AAFITRANS (M. Beroiz et al. 2020; P. Joseph 2023); ASTROMETRY.NET (D. Lang et al. 2010); ASTROPY (Astropy Collaboration et al. 2013, 2018, 2022); CURVIT

(P. Joseph et al. 2021); JUPYTER (T. Kluyver et al. 2016); MATPLOTLIB (J. D. Hunter 2007); NUMPY (C. R. Harris et al. 2020); PANDAS (The pandas development team 2020); PHOTUTILS (L. Bradley et al. 2022); SAOIMAGEDS9 (W. A. Joye & E. Mandel 2003); SCIPY (P. Virtanen et al. 2020); SPYDER (P. Raybaut 2009); TOPCAT (M. B. Taylor 2005).

Appendix A
Image Binning and Rescaling

Here, we define the image binning and rescaling operations used in Appendices B and C. Let A_{xy} denote a given pixel in the xth column and yth row in the original image. If the original image is binned using binning factors m and n pixels along the horizontal and vertical directions, respectively, then the binned pixel B_{ij} in the ith column and jth row in the binned image can be represented by the equation

$$B_{ij} = \frac{1}{m \times n} \sum_{x=(i-1).m+1}^{i.m} \sum_{y=(j-1).n+1}^{j.n} A_{xy}. \tag{A1}$$

The binned image constructed using Equation (A1) can be rescaled back to the original dimension by repeating the binned pixel m and n times along the horizontal and vertical directions, respectively. Let B_{xy} denote a given pixel in the xth column and yth row in the binned image. The rescaled pixel R_{ij} in the ith column and jth row in the rescaled image can be represented by the equation

$$R_{ij} = B_{xy} \tag{A2}$$

$$\text{where, } x = \left\lfloor \frac{i-1}{m} \right\rfloor + 1, \tag{A3}$$

$$y = \left\lfloor \frac{j-1}{n} \right\rfloor + 1, \tag{A4}$$

with m and n being the rescaling factors.

In this study, we have kept $m = n$ during binning and rescaling operations using Equations (A1) and (A2). Additionally, the rescaling factors were kept equal to the binning factors.

Appendix B
Background Map Generation

The UVIT images have relatively low background noise levels compared to the visible or infrared images, but we still need to correct the background to obtain accurate photometry. The background may vary in time and across the field of view. Only large-scale and smooth background variations are expected across the field of view in each image. While estimating the background levels from a visually selected nearby background region for each source in every episode image is possible, it is an inefficient and involving method while working with multiple sources and images.

Therefore, we developed a method to generate 2D background maps for the episode images. To create a background map, the common method adopted for optical imaging data involves placing an appropriately sized grid on the input image, taking the mean, median, or another statistic of each grid box to get the local background levels and then interpolating the resulting low-resolution background map to match the input image resolution, with some form of filtering to suppress the under- or overestimation of the background levels. We have adopted this method with the median as the background estimator to generate the background maps but with some modifications to account for the Poisson distribution of the background count levels of the UVIT images. A description of our background map generation method is given below.

The UVIT background count distribution is Poisson, which can be represented by the following equation:

$$P(X = k) = \frac{\lambda^k e^{-\lambda}}{k!}, \tag{B1}$$

where X is a discrete random variable that represents the background counts per pixel, λ is the expected value, and $P(X = k)$ gives the probability of X being equal to k. Although λ can be obtained by taking the mean of the distribution, the mean is highly influenced by outliers present in the real data. Therefore, we want to use the median to estimate λ as it is resistant to outliers. However, the median cannot be used to estimate λ when λ is small (for example, the median might be almost always zero when $\lambda = 0.5$). For larger values of λ ($\lambda \geqslant 10$), the shape of the Poisson distribution resembles that of the normal form and can be approximated to be a Gaussian distribution. Such a Gaussian approximation of the Poisson distribution is useful because both the median and mean are equal to the expected value for a Gaussian distribution; therefore, we can use the median to estimate λ when this criterion is met.

To understand the uncertainties involved in using the median to estimate λ, we use the sharp bounds of the Poisson distribution median given by K. P. Choi (1994):

$$\lambda - \ln(2) \leqslant \nu < \lambda + \frac{1}{3}, \tag{B2}$$

where ν is the median of the Poisson distribution. The above equation suggests that taking the median as the Poisson expected value λ will have an absolute uncertainty of $\sim 100/\lambda$ %. For example, when $\lambda = 10$, the median will be close to λ with a possible ~10% error. The uncertainty becomes ~5% when $\lambda = 20$. As λ becomes large, the error reduces, and the median becomes very close to λ.

Consequently, we need $\lambda \approx 10$ to use the median approximation with a ~10% or better uncertainty. However, $\lambda < 10$ for all our episode images; the average photon count rate is $\sim 5 \times 10^{-5}$ CPS per subpixel for the NGC 188 F148W filter images, and λ remains low even for those images with ~2000 s exposure time (λ = background count rate × exposure time). To overcome this problem, we made $\lambda \geqslant 10$ by binning the image subpixels using Equation (A1) along the x- and y-directions to generate a "superpixel." Binning of the subpixels increases the background count rate per superpixel. The binning factor b was computed such that $\lambda \geqslant 10$ using the equation

$$b \geqslant \sqrt{\frac{10}{t_{\text{exp}} \times \text{CPS}_{\text{bkg}}}}, \tag{B3}$$

where CPS_{bkg} is the approximate background count rate in CPS and t_{exp} is the exposure time in seconds. Since we have images with exposure times as low as ~100 s, we used $t_{\text{exp}} = 100$ and $\text{CPS}_{\text{bkg}} = 5 \times 10^{-5}$ in Equation (B3) and obtained $b \approx 45$. We adopted a larger binning factor of 64

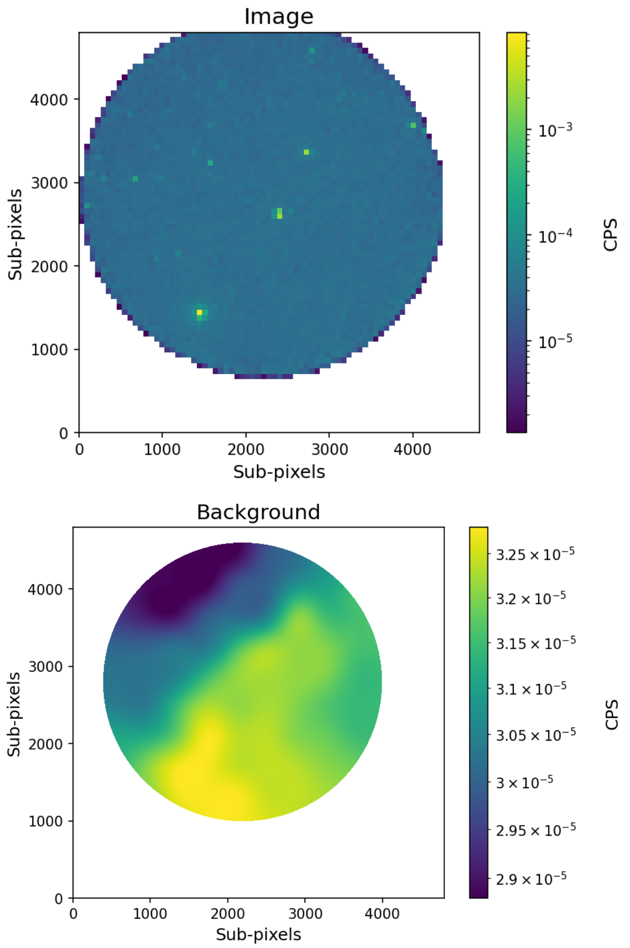
Image

Background

Figure 6. The binned and rescaled image (top panel) and the background map (bottom panel).

because we want to use binning factors that are powers of two for ease of dealing with the UVIT imaging data.

The UVIT FITS images are in the CPS unit and have a size of 4800×4800 subpixels. We binned all episode images with a binning factor of 64 using Equation (A1), resulting in binned images with sizes of 75×75 superpixels. Now, the background count distribution across the superpixels corresponds to $\lambda \geqslant 10$ even for an exposure time as low as 100 s. The binned images were rescaled to the 4800×4800 dimension using Equation (A2) so that the background maps derived from the rescaled images would match the size of the input images. Background maps were generated from each rescaled image using the `Background2D` function from the `Photutils` package (L. Bradley et al. 2022). We used a grid box size of 384×384 subpixels (6×6 superpixels) and found the median background level in each grid box.

We restricted the background maps to a radius of 1800 subpixels from the centroid of the images for the NGC 188 data. The top and bottom panels in Figure 6 show a sample rescaled NGC 188 image and corresponding background map, respectively. The spread in the background levels (maximum–minimum background) across the field of view is $\sim 0.5 \times 10^{-5}$ CPS for all NGC 188 background maps. In the case of HZ 4, the background maps were restricted to boxes of 1500×1500 subpixels centered on the image centroids. We found a background spread of $\sim 0.2 \times 10^{-5}$ CPS in HZ 4. The background variations across NGC 188 and HZ 4 episode images are given in Appendix F. HZ 4 UVIT images have higher FUV background levels than most NGC 188 images (this is also true for Galaxy Evolution Explorer GALEX, FUV imaging of these sources). The relatively high-background levels observed in some episodes of NGC 188 data are discussed in Appendix F.

A Poisson treatment of the UVIT background can also be found in B. Ananthamoorthy et al. (2024).

Appendix C
Source Detection

We detected sources in the UVIT episode images using the DAOFIND algorithm implemented in the `Photutils` package (P. B. Stetson 1987; L. Bradley et al. 2022). To improve source detectability, the episode images were preprocessed as follows.

Each episode image in 4800×4800 subpixels was binned by a factor of 2 using Equation (A1) to create an image in 2400×2400 binned-pixels. The binned image was convolved with a 2D Gaussian kernel having a standard deviation of 1.5 binned-pixels, resulting in a smoothed binned image with reduced noise levels. The source detectability is improved due to the increased signal-to-noise ratio per binned pixel, with a slight reduction in the detected source centroid accuracy. The smoothed binned image was rescaled back to the original 4800×4800 dimension following Equation (A2) using a rescaling factor of 2.

DAOFIND was run on the preprocessed images to detect sources. The DAOFIND source detection threshold was $\kappa \times B$, where B is the median value of the background map and κ is a constant. κ was varied in the NGC 188 images such that 20–200 source detections were made, while $\kappa = 40$ was used for all HZ 4 images. To avoid mistaking the noisy pixels at the edges as sources, we confined our detections in the NGC 188 images to a circular region of 1800 pixels. The center of this circular region is determined by taking the centroid of the 2D background array, which was calculated by taking the weighted sum of all the x and y pixel coordinates. Since the centroid was estimated from the image background, large background variations can cause the centroid to shift toward the denser background regions. However, there were no such large background variations in our input images. In the case of HZ 4, the detections were restricted to boxes of 1500×1500 subpixels centered on the image centroids.

Appendix D
Flux Measurements and Uncertainties

The corrected flux measurements and their associated uncertainties for HZ 4 and the three NGC 188 candidates used in Section 4 are presented here. Tables 5 and 6 list the measurements for HZ 4 and the NGC 188 candidates, respectively.

Table 5
Corrected Flux Measurements and Associated Uncertainties for HZ 4 as Shown in Figure 4

No.	Observation ID	Time (MJD)	Source Flux (CPS)	Error (CPS)
1.	C02_002T01_9000000888	57738.420	23.385	0.259
		57738.424	23.756	0.261
		57738.428	24.361	0.264
2.	C03_013T01_9000001586	58032.171	23.606	0.275
		58032.239	23.874	0.261
		58032.242	23.873	0.313
		58032.306	23.448	0.321
3.	C04_010T01_9000003158	58738.384	23.847	0.267
		58738.389	22.915	0.262
		58738.393	23.481	0.305
		58738.451	23.330	0.390
4.	C02_002T01_9000006092	60364.549	23.574	0.265
		60364.554	23.481	0.265

Table 6
Corrected Flux Measurements and Associated Uncertainties for the Three NGC 188 Candidates as Shown in Figure 5

No.	Observation ID	Time	Candidate 1		Candidate 2		Candidate 3	
		(MJD)	(CPS)		(CPS)		(CPS)	
			Source Flux	Error	Source Flux	Error	Source Flux	Error
1.	T01_034T01_9000000392	57469.571	16.918	0.171	11.044	0.140	0.864	0.042
		57469.625	17.676	0.192	11.161	0.154	0.888	0.047
2.	G05_209T01_9000000458	57526.814	17.132	0.123	11.250	0.101	0.896	0.031
3.	G05_258T01_9000000666	57646.251	17.391	0.165	11.072	0.133	0.942	0.042
4.	C02_016T01_9000000992	57783.494	17.281	0.118	11.437	0.098	0.995	0.031
5.	C02_030T01_9000001168	57859.093	17.401	0.234	11.395	0.192	0.899	0.059
		57859.214	17.405	0.197	11.305	0.161	0.893	0.049
		57859.284	16.637	0.214	11.155	0.178	0.837	0.053
6.	C03_015T01_9000001788	58108.584	16.984	0.333	10.929	0.271	0.869	0.083
7.	T02_002T01_9000001914	58172.451	17.349	0.095	11.149	0.077	0.947	0.024
		58172.514	17.227	0.127	11.099	0.103	0.914	0.032
8.	C03_015T02_9000002008	58212.229	17.203	0.197	11.061	0.160	0.958	0.051
9.	C03_015T04_9000002240	58319.753	17.361	0.126	11.009	0.102	0.937	0.032
10.	C03_015T04_9000002328	58356.101	16.804	0.253	10.707	0.205	0.965	0.066
		58356.218	17.270	0.223	11.168	0.182	0.955	0.058
		58356.286	17.472	0.177	11.134	0.143	0.871	0.043
11.	C03_015T03_9000002366	58375.045	17.445	0.175	10.634	0.139	0.898	0.043
		58375.096	17.558	0.200	11.204	0.162	0.889	0.049
		58375.115	17.528	0.331	10.473	0.261	0.812	0.079
12.	C03_015T04_9000002382	58382.886	17.197	0.121	11.229	0.099	0.894	0.030
13.	C04_009T01_9000002448	58414.413	17.227	0.121	10.992	0.098	0.942	0.031
14.	C04_009T02_9000002618	58487.772	17.469	0.122	11.453	0.100	0.967	0.031
15.	C05_013T02_9000003364	58830.612	17.365	0.121	11.083	0.098	0.940	0.031
16.	C05_013T03_9000003376	58836.904	17.505	0.183	10.701	0.145	0.875	0.045
17.	C05_013T04_9000003660	58981.357	17.120	0.120	11.174	0.099	0.939	0.031
18.	T03_247T01_9000003914	59127.105	17.363	0.295	11.086	0.240	0.943	0.076
		59127.155	17.730	0.177	11.331	0.144	0.856	0.043

Table 6
(Continued)

No.	Observation ID	Time	Candidate 1 (CPS)		Candidate 2 (CPS)		Candidate 3 (CPS)	
		(MJD)	Source Flux	Error	Source Flux	Error	Source Flux	Error
19.	C05_013T06_9000003920	59137.921	17.053	0.150	10.965	0.122	0.876	0.037
20.	C06_010T01_9000004504	59398.264	16.841	0.155	10.623	0.125	0.879	0.039
21.	C06_010T02_9000004618	59428.848	16.879	0.105	10.699	0.085	0.884	0.026
		59428.915	16.654	0.136	10.613	0.110	0.876	0.034
22.	C06_010T03_9000004672	59453.406	16.707	0.128	10.899	0.105	0.851	0.032
		59453.472	16.839	0.105	10.785	0.085	0.870	0.026
23.	C06_010T05_9000004736	59512.332	16.711	0.102	11.159	0.084	0.929	0.026
		59512.392	16.837	0.283	11.185	0.233	0.965	0.074
24.	T04_065T01_9000004750	59519.236	16.528	0.313	11.743	0.267	0.906	0.080
25.	C06_010T05_9000005424	59928.218	16.590	0.183	11.191	0.152	0.979	0.048
		59928.284	16.451	0.110	10.905	0.091	0.922	0.028
		59928.350	16.584	0.128	11.029	0.106	0.941	0.033
26.	C06_010T05_9000005436	59936.404	16.347	0.123	10.845	0.102	0.890	0.031
		59936.470	16.871	0.097	10.726	0.079	0.917	0.025
27.	C06_010T05_9000005484	59959.873	17.005	0.107	11.026	0.088	0.909	0.027
		59959.942	17.019	0.119	11.073	0.097	0.939	0.031
28.	T05_101T01_9000005578	60056.976	17.022	0.144	11.030	0.118	0.946	0.037
		60057.043	17.278	0.281	10.812	0.226	1.055	0.076
29.	T05_101T01_9000005586	60062.993	17.361	0.141	10.681	0.112	0.895	0.035
		60063.062	16.668	0.298	10.662	0.242	0.889	0.076
30.	C06_010T05_9000005670	60094.024	16.676	0.176	10.553	0.142	0.943	0.046
		60094.215	16.507	0.134	10.408	0.109	0.867	0.035
31.	C06_010T01_9000005800	60154.930	16.300	0.112	10.018	0.089	0.838	0.028
		60154.996	16.870	0.268	10.077	0.211	0.901	0.068
32.	C06_010T01_9000005816	60169.397	15.978	0.282	10.260	0.230	0.834	0.070
		60169.451	16.119	0.201	10.615	0.166	0.764	0.050
33.	C09_011T02_9000006310	60485.733	15.926	0.145	9.963	0.117	0.774	0.036
34.	C09_011T03_9000006410	60547.257	15.994	0.146	10.126	0.118	0.828	0.037
		60547.323	15.872	0.106	10.190	0.086	0.876	0.028
35.	C09_011T01_9000006418	60550.356	15.891	0.165	10.174	0.134	0.825	0.043

Appendix E
Building Astrometry.net Index Files for UVIT

This appendix provides information on the custom-made index files used to perform astrometry on the UVIT images. We had limitations in using the index files provided by Astrometry.net.[7] The 5200 series index files, generated from visible channel catalogs, failed to provide astrometric solutions in many of the UVIT images. The relatively lower spatial resolution of GALEX compared to UVIT affected the astrometric accuracy when 6000 and 6100 series index files were used. Therefore, new index files were generated using `Astrometry.net` software (D. Lang et al. 2010) from a subset of the Gaia Data Release 3 (DR3) catalog (Gaia Collaboration et al. 2016, 2023). This subset contains blue and bright sources that are expected to be visible in the UVIT images, and the derived index files are suitable for astrometry on UV images. The steps followed to build the index files are provided in the following subsections.

E.1. Creating the Subset Catalog

The first step in the index files generation process was to create a subset of the Gaia DR3 catalog (subset catalog) that contains blue and bright sources. The source-selection criterion to generate the subset catalog was established using the UVIT Small Magellanic Cloud (SMC) catalog that contains 11,241 point sources (A. Devaraj et al. 2023). The celestial coordinates (α, δ) of the UVIT SMC catalog sources were cross-matched with those of the Gaia DR3 catalog, and it resulted in a matched list of 10,784 sources (96% of the SMC catalog sources). The histograms in Figure 7 depict the Gaia

---

[7] http://data.astrometry.net/

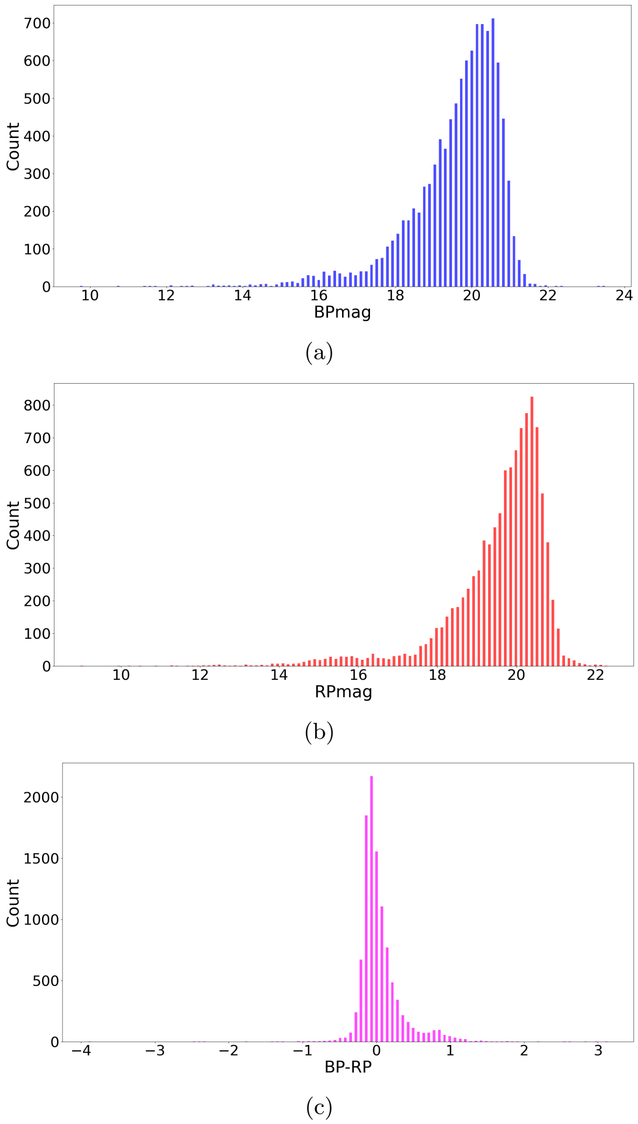

(a)

(b)

(c)

Figure 7. The three-paneled plot represents the distribution of the sources in the UVIT SMC catalog cross-matched with the Gaia catalog in terms of BPmag, RPmag, and $BP - RP$.

blue passband magnitude (BPmag), red passband magnitude (RPmag), and BPmag – RPmag color ($BP - RP$) distribution of the UVIT SMC-Gaia DR3 matched sources. From a visual inspection of the histograms and multiple trials, the following source-selection criterion was finalized:

$$\begin{aligned} &(\text{BPmag} <= 12) \quad \text{OR} \\ &(BP - RP <= 0.8 \quad \text{AND} \quad \text{BPmag} <= 21). \end{aligned} \tag{E1}$$

Table 7 shows the percentage of sources falling under each part of the source-selection criteria for the UVIT SMC-Gaia DR3 matched catalog. The whole Gaia DR3 catalog gave a list of 64,597,375 sources that matched our source-selection criteria. The data for these sources were downloaded for the J2000 reference epoch from one of Gaia's partner data centers, Centre de Donnés astronomiques de Strasbourg.[8] The subset catalog was then sorted based on the BPmag column in ascending order and converted into the FITS table format.

Table 7
Percentage of Sources Falling under Each Part of the Source-selection Criteria for the UVIT SMC-Gaia DR3 Matched Catalog

Criteria	Source
BPmag $\leqslant$ 12	0.046%
BPmag $\leqslant$ 21	94.807%
BP-RP $\leqslant$ 0.8	94.371%
($BP - RP \leqslant$ 0.8) AND (BPmag $\leqslant$ 21)	91.747%

E.2. Generating the Index Files

The subset catalog was divided into 48 FITS tables, corresponding to the 48 HEALPix equal-area subdivisions of the sky. This division was achieved using the `hsplit` command from `Astrometry.net`, which uses the α and δ column values of the subset catalog to split the sky into equal-area subdivisions according to the HEALPix specification (K. M. Górski et al. 2005). Subsequently, the `build-astrometry-index` command was used to generate index files from each of the 48 FITS tables. During the index file generation, we selected `build-astrometry-index` preset values from 1 to 9, which generates index files that contain features of different angular sizes. This selection led to the creation of 9 index files for each of the 48 HEALpix tiles, each corresponding to a different scale, resulting in 432 UVIT index files. Using these, we were able to obtain the astrometric solution for the UVIT images of NGC 188. The generated index files will be generally useful for obtaining astrometric solutions for UVIT images.

Appendix F
Cases of High Background Observed in the UVIT Images

This section presents our findings regarding relatively high-background levels in recent NGC 188 episode images. For every input image, we estimated the background enclosed under a 12 subpixel radius aperture by multiplying the image background map median value, B, with a factor of $\pi \times 12^2$. These background levels are shown in Figure 8 for HZ 4 and NGC 188. Notably, the most recent NGC 188 episode images exhibit significant variations in background levels. HZ 4 episode images have a higher background level than most NGC 188 episode images. GALEX imaging of HZ 4 similarly shows elevated background levels relative to GALEX imaging of NGC 188. Such sky-location-dependent variations in UV background levels are known (R. C. Henry et al. 2014).

F.1. Temporal Variation of the Background

We checked whether the background exhibited spatial or temporal variations within the affected episodes. To study the temporal variations, we used `Curvit` (P. Joseph et al. 2021) to produce light curves for the background regions. The background regions were selected through visual inspection. We generated background light curves using a 300 subpixel radius aperture and a time bin of 50 s. Figure 9 shows the background light curves for a high-background episode and the preceding normal background episode in observation ID C06_010T05_9000005670. In the figure, the top panel corresponds to the preceding episode with a normal background, while the middle panel depicts the high-background episode. On the left side of the panel, the selected background region in the UVIT image field is highlighted by a 300

---

[8] https://cds.unistra.fr/

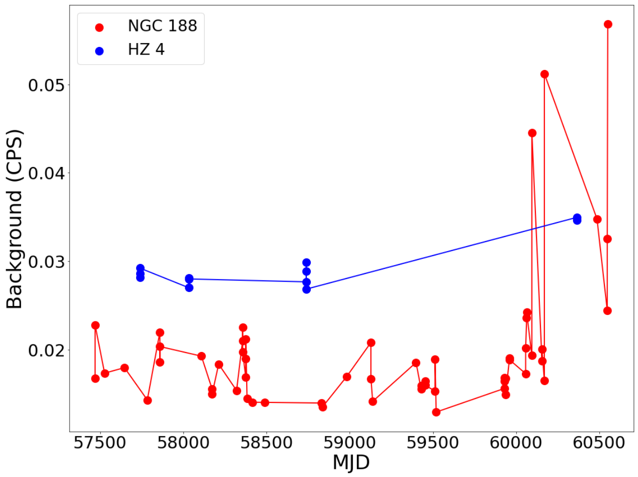

Figure 8. Median background levels corresponding to a 12 subpixel radius aperture in the F148W images of NGC 188 and HZ 4 across different episodes.

subpixel radius aperture, and the corresponding light curve is displayed on the right side. In the high-background episode, the background varies, with the levels being high initially and then reducing over time. No such large background variation was observed in the normal background episode. Temporal variations in background levels were found in all six episodes with relatively high-background levels.

To determine whether the elevated background levels were spatially localized, we placed six smaller apertures, each with a 100 subpixel radius, in randomly selected background regions of the high-background UVIT episodes. Light curves were generated for these regions, as shown in the bottom panel of Figure 9. In high-background episodes, the background flux variations across the different regions were consistent. This consistency indicates that the elevated background levels are not confined to specific areas and are a widespread feature across the image.

As per the AstroSat Handbook (Version: 1.10),[9] possible sources that can contribute to the UVIT background include the bright limb of the Earth, zodiacal light, and geocoronal lines during daytime observations. Our preliminary checks suggest that the background levels are varying depending on the position of the spacecraft in orbit. Notably, the rise in background levels coincides with the solar cycle 25 maximum. A detailed analysis of background variations will be presented in a separate study.

---

[9] https://www.issdc.gov.in/astro.html

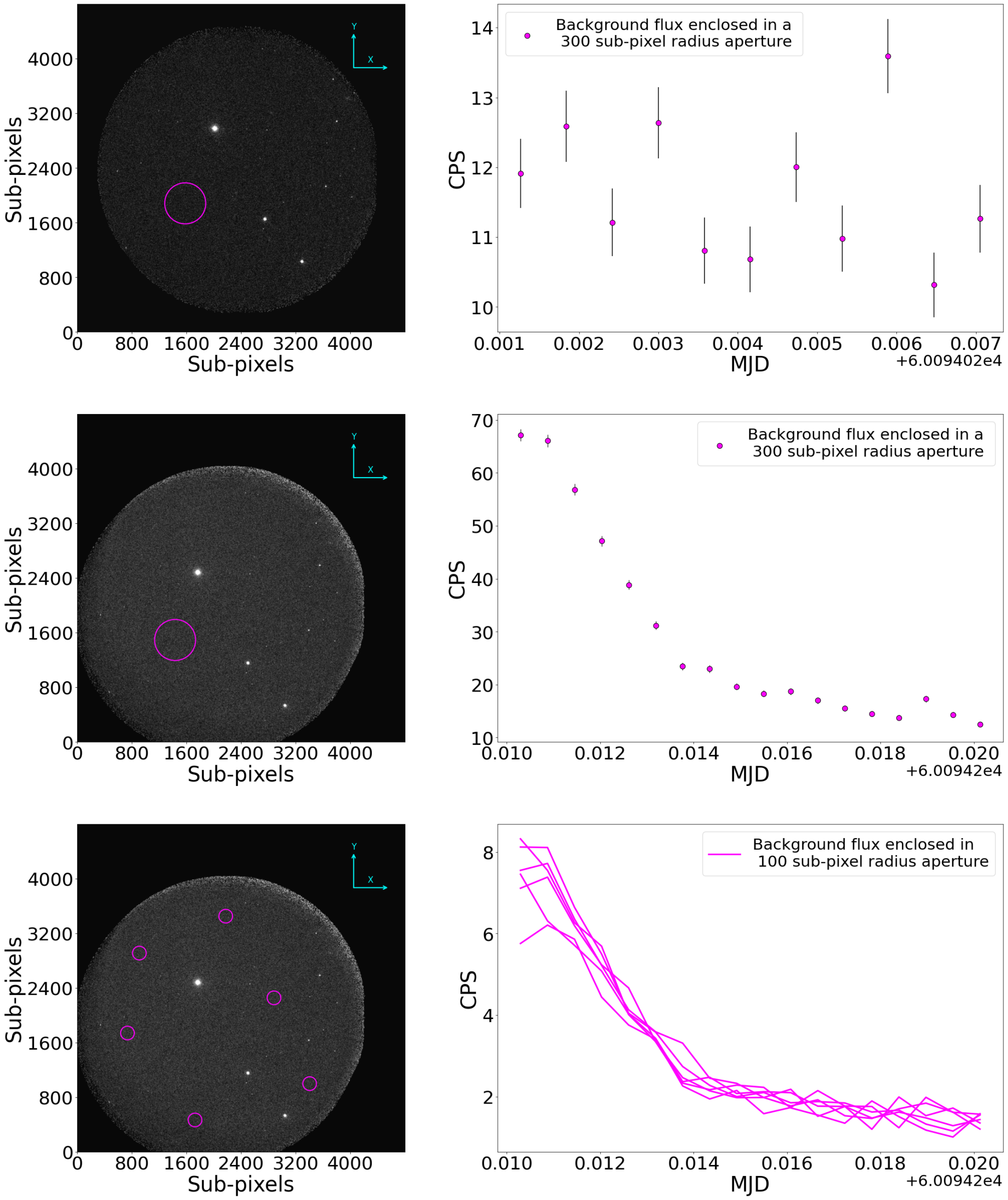

Figure 9. The three-paneled subplot shows the temporal variation of the background flux for the episodes from observation ID C06_010T05_9000005670. The middle and bottom panels display episodes with high-background levels, while the top panel shows the preceding episode with normal background levels. On the left side of each panel, the UVIT F148W image in instrument coordinates highlights the selected background regions, marked by circular apertures. The corresponding light curves for these regions are shown on the right side of each panel.

ORCID iDs

Akanksha Dagore https://orcid.org/0009-0001-5407-3016
Prajwel Joseph https://orcid.org/0000-0003-1409-1903
Annapurni Subramaniam https://orcid.org/0000-0003-4612-620X
C. S. Stalin https://orcid.org/0000-0002-4998-1861

References

Agrawal, P. 2017, JApA, 38, 27

Ananthamoorthy, B., Bhattacharya, D., Sreekumar, P., & Swathi, B. 2024, AJ, 168, 22

Astropy Collaboration, Price-Whelan, A. M., Lim, P. L., et al. 2022, ApJ, 935, 167

Astropy Collaboration, Price-Whelan, A. M., Sipőcz, B. M., et al. 2018, AJ, 156, 123

Astropy Collaboration, Robitaille, T. P., Tollerud, E. J., et al. 2013, A&A, 558, A33

Banks, B., Miller, S., & de Groh, K. 2004, in 2nd Int. Energy Conversion Engineering Conf., 5638

Beroiz, M., Cabral, J., & Sanchez, B. 2020, A&C, 32, 100384

Bradley, L., Sipőcz, B., Robitaille, T., et al. 2022, astropy/photutils: v1.5.0, Zenodo, doi:10.5281/zenodo.6825092

Choi, K. P. 1994, Proc. Amer. Math. Soc., 121, 245

Dagore, A., Joseph, P., Tandon, S., et al. 2025, Data and software for "Nine years of UVIT: assessing sensitivity variation", v1.0.1, Zenodo, doi:10.5281/zenodo.18076974

Devaraj, A., Joseph, P., Stalin, C. S., Tandon, S. N., & Ghosh, S. K. 2023, ApJ, 946, 65

Gaia Collaboration, Prusti, T., de Bruijne, J., H., J., et al. 2016, A&A, 595, A1

Gaia Collaboration, Vallenari, A., Brown, A. G. A., et al. 2023, A&A, 674, A1

Garoli, D., Rodriguez De Marcos, L. V., Larruquert, J. I., et al. 2020, ApSci, 10, 7538

Ghosh, S. K., Tandon, S. N., Joseph, P., et al. 2021, JApA, 42, 29

Ghosh, S. K., Tandon, S. N., Singh, S. K., et al. 2022, JApA, 43, 77

Górski, K. M., Hivon, E., Banday, A. J., et al. 2005, ApJ, 622, 759

Harris, C. R., Millman, K. J., van der Walt, S. J., et al. 2020, Natur, 585, 357

Henry, R. C., Murthy, J., Overduin, J., & Tyler, J. 2014, ApJ, 798, 14

Hunter, J. D. 2007, CSE, 9, 90

Joseph, P. 2023, prajwel/aafitrans: v0.2.1, Zenodo, doi:10.5281/zenodo.10041152

Joseph, P., Stalin, C. S., Tandon, S. N., & Ghosh, S. K. 2021, JApA, 42, 25

Joye, W. A., & Mandel, E. 2003, ASPC, 295, 489

Kluyver, T., Ragan-Kelley, B., Pérez, F., et al. 2016, in Positioning and Power in Academic Publishing: Players, Agents and Agendas, ed. F. Loizides & B. Schmidt (IOS Press), 87

Lang, D., Hogg, D. W., Mierle, K., Blanton, M., & Roweis, S. 2010, AJ, 139, 1782

Nahor, G., Baer, M. G., Anholt, M., et al. 1993, SPIE, 1971, 288

Rani, S., Subramaniam, A., Pandey, S., et al. 2021, JApA, 42, 47

Raybaut, P. 2009, pythonhosted.org

Singh, K. P., Tandon, S. N., Agrawal, P. C., et al. 2014, SPIE, 9144, 91441S

Stetson, P. B. 1987, PASP, 99, 191

Subramaniam, A., Sindhu, N., Tandon, S. N., et al. 2016, ApJ, 833, L27

Tandon, S. N., Postma, J., Joseph, P., et al. 2020, AJ, 159, 158

Tandon, S. N., Subramaniam, A., Girish, V., et al. 2017, AJ, 154, 128

Taylor, M. B. 2005, ASPC, 347, 29

The pandas development team 2020, pandas-dev/pandas: Pandas, v3.0.0, Zenodo, doi:10.5281/zenodo.3509134

Virtanen, P., Gommers, R., Oliphant, T. E., et al. 2020, NatMe, 17, 261

Wenger, M., Ochsenbein, F., Egret, D., et al. 2000, A&AS, 143, 9